ACSNANO

www.acsnano.org

ARTICLE

Interlayer Coupling in Twisted WSe_2/WS_2 Bilayer Heterostructures Revealed by Optical Spectroscopy

Kai Wang,*[,†] Bing Huang,[†,‡,§] Mengkun Tian,[∥] Frank Ceballos,[⊥] Ming-Wei Lin,[†] Masoud Mahjouri-Samani,[†] Abdelaziz Boulesbaa,[†] Alexander A. Puretzky,[†] Christopher M. Rouleau,[†] Mina Yoon,[†] Hui Zhao,[⊥] Kai Xiao,[†] Gerd Duscher,[∥] and David B. Geohegan*[,†]

[†]Center for Nanophase Materials Sciences, Oak Ridge National Laboratory, Oak Ridge, Tennessee 37831 United States
[‡]Beijing Computational Science Research Center, Beijing 100094, China
[§]Department of Materials Science and Engineering, University of Utah, Salt Lake City, Utah 84112, United States
[∥]Department of Materials Science and Engineering, University of Tennessee, Knoxville, Tennessee 37996 United States
[⊥]Department of Physics and Astronomy, The University of Kansas, Lawrence, Kansas 66045 United States

Supporting Information

ABSTRACT: van der Waals (vdW) heterostructures are promising building blocks for future ultrathin electronics. Fabricating vdW heterostructures by stamping monolayers at arbitrary angles provides an additional range of flexibility to tailor the resulting properties than could be expected by direct growth. Here, we report fabrication and comprehensive characterizations of WSe_2/WS_2 bilayer heterojunctions with various twist angles that were synthesized by artificially stacking monolayers of WS_2 and WSe_2 grown by chemical vapor deposition. After annealing the WSe_2/WS_2 bilayers, Raman spectroscopy reveals interlayer coupling with the appearance of a mode at 309.4 cm^{-1} that is sensitive to the number of WSe_2 layers. This interlayer coupling is associated with substantial quenching of the intralayer photoluminescence. In addition, microabsorption spectroscopy of WSe_2/WS_2 bilayers revealed spectral broadening and shifts as well as a net ~10% enhancement in integrated absorption strength across the visible spectrum with respect to the sum of the individual monolayer spectra. The observed broadening of the WSe_2 A exciton absorption band in the bilayers suggests fast charge separation between the layers, which was supported by direct femtosecond pump−probe spectroscopy. Density functional calculations of the band structures of the bilayers at different twist angles and interlayer distances found robust type II heterojunctions at all twist angles, and predicted variations in band gap for particular atomistic arrangements. Although interlayer excitons were indicated using femtosecond pump−probe spectroscopy, photoluminescence and absorption spectroscopies did not show any evidence of them, suggesting that the interlayer exciton transition is very weak. However, the interlayer coupling for the WSe_2/WS_2 bilayer heterojunctions indicated by substantial PL quenching, enhanced absorption, and rapid charge transfer was found to be insensitive to the relative twist angle, indicating that stamping provides a robust approach to realize reliable optoelectronics.

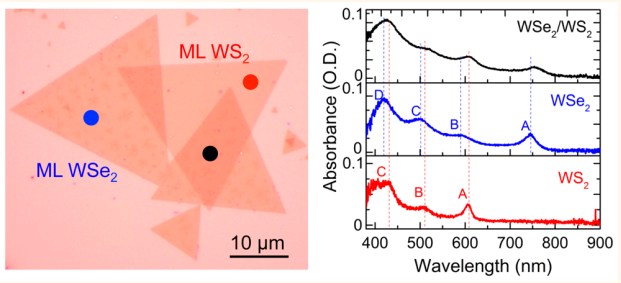

KEYWORDS: *van der Waals heterostructures, interlayer coupling, twist angle, charge transfer*

As direct band gap semiconductors, monolayers (MLs) of transition-metal dichalcogenides (TMDs) exhibit exotic properties that arise from quantum confinement and crystal symmetry effects in the two-dimensional (2D) limit.[1,2] Several functional devices with extraordinary performance, such as field-effect transistors with excellent on/off ratios,[3] chemical sensors with high sensitivity,[4] ML semiconductor lasers with ultralow threshold,[5] and atomically thin piezoelectric generators,[6,7] have been demonstrated with TMD MLs. Stacking two different TMD MLs leads to a type II heterobilayer with a van der Waals (vdW) interface that possesses novel optical and transport properties with a rich variety of device physics, such as long-lived interlayer excitons (~1.8 ns) and ultrafast charge transfer (~50 fs) at the

Received: February 29, 2016
Accepted: June 16, 2016
Published: June 16, 2016

DOI: 10.1021/acsnano.6b01486
ACS Nano 2016, 10, 6612−6622

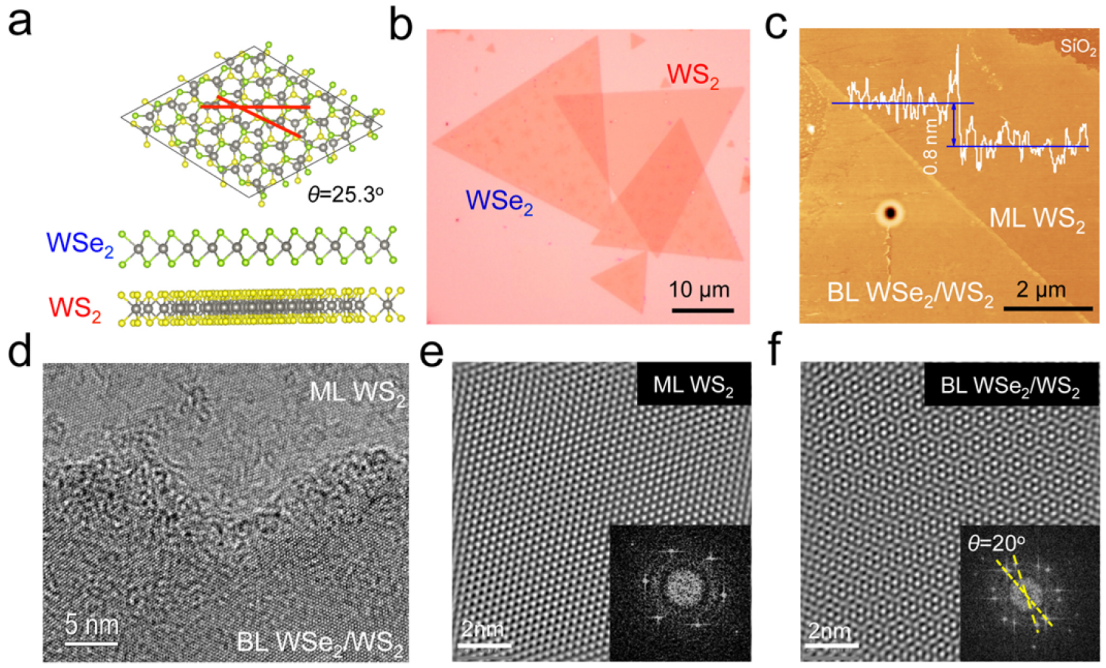

Figure 1. Structural analysis of WSe_2/WS_2 BLs. (a) Illustration of a WSe_2/WS_2 BL assembled from ML WSe_2 stacked on ML WS_2 with a twist angle of 25.3°. (b) Optical microscope image of WSe_2 MLs, WS_2 MLs, and WSe_2/WS_2 BLs on a SiO_2/Si substrate. (c) Representative AFM image of a WSe_2/WS_2 BL and the corresponding height profile of ML WS_2 on ML WSe_2. (d) HRTEM image taken from WSe_2/WS_2 BL. (e and f) FFT filtered images of ML WS_2 and WSe_2/WS_2 BL in (d). Insets in (e) and (f) show the corresponding FFT patterns.

interface.[8,9] Notably, stacking orientation, *i.e.*, the mutual twist angle between two MLs, significantly influences the interlayer coupling at the interface, and suggests the possibility of tailoring the electronic structure of the bilayer by simply varying the twist angles, as in the case of bilayers of graphene and TMDs.[10−12]

Recently, a number of TMD heterobilayers have been reported, such as MoS_2/WSe_2,[13,14] MoS_2/WS_2,[15,16] $MoSe_2/WSe_2$,[17,18] and $MoS_2/MoSe_2$,[17,19] and two approaches were used in their fabrication: stamping of MLs of exfoliated[14,18,20,21] or chemical vapor deposition (CVD)-grown TMDs[15,16,22] and direct growth of bilayers (BLs) by CVD.[23,24] Although stamping of exfoliated materials produces BLs with superior crystal quality compared to BLs stamped from CVD-grown MLs, considerable effort using second-harmonic generation (SHG),[18,22] for example, is required to determine the mutual crystal orientations or angular twist of the MLs. Consequently, CVD remains an efficient technique to produce large-area high-quality TMD MLs with well-defined triangular or truncated triangular crystal shapes[25,26] that are easily interrogated by optical or atomic force microscopy (AFM) to determine twist angle. However, direct CVD synthesis of heterobilayers *via* vdW epitaxial growth is technically challenging due to chalcogen interdiffusion (*e.g.*, sulfur and selenium) at elevated growth temperatures and lattice mismatch between the layers, and such attempts normally result in the growth of either alloyed MLs or lateral heterojunctions.[27,28] Of those cases that do result in a bilayer, only stable stacking configurations are produced, typically limiting the twist angles to 0°or 60° for heterobilayers with small lattice mismatch[23,29] or other specific angles for large lattice match combinations.[30,31]

A WSe_2/WS_2 BL is of high interest for optoelectronic applications due to (1) recent theoretical predictions of direct band gap (~1.0 eV) interlayer excitons for A−B stacking,[32] (2) high photoluminescence (PL) quantum yield for both WS_2 and WSe_2 MLs that is 2 orders of magnitude larger than that of MoS_2 MLs at room temperature,[33] and (3) high hole mobility (~100 $cm^2\ V^{-1}\ s^{-1}$) in WSe_2 even at a thickness of 1 ML.[34] Therefore, stacking of WS_2 and WSe_2 MLs holds great promise for p−n heterojunctions to perhaps pave the way for future applications in optoelectronic devices. However, the dependence of WSe_2/WS_2 BLs optical properties on twist angle, a relationship that was studied in initial attempts in $MoS_2/MoSe_2$ MLs,[17] is not typically explored in the majority of the BL families. Here we report fabrication and detailed characterization of BLs of WSe_2/WS_2 with different twist angles produced by artificially stacking large (up to 50 μm) CVD-grown WS_2 and WSe_2 MLs on sapphire and SiO_2/Si substrates. The interlayer interactions in the heterobilayers were probed by a combination of optical spectroscopies including low-frequency (LF) Raman spectroscopy, absorption, photoluminescence, and femtosecond transient absorption spectroscopy. The Raman spectra of WSe_2/WS_2 BLs show new peaks corresponding to a layer-number-sensitive mode of WS_2 at 309.4 cm^{-1}, indicating layer coupling after annealing. We show that this feature is corroborated by microabsorption and PL measurements indicating charge transfer, the time scale of which (<450 fs) is supported by direct femtosecond pump−probe spectroscopy. Although density functional theory (DFT) calculations predicted the band structure characteristics of BLs at the particular atomistic arrangements, and the charge transfer dynamics indicated the formation of an interlayer exciton, the interlayer coupling probed by optical spectroscopy was found relatively insensitive to the twist angle, suggesting stamping is a robust approach to fabricate reliable optoelectronics based on vdW heterostructures.

DOI: 10.1021/acsnano.6b01486
ACS Nano 2016, 10, 6612−6622

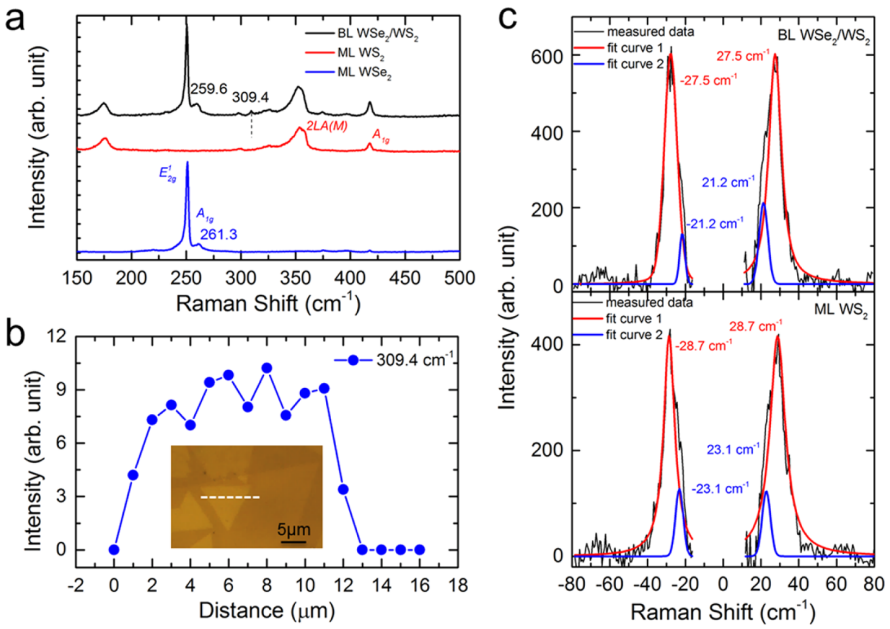

Figure 2. Raman spectra analysis of WSe_2/WS_2 BLs. (a) Raman spectra of ML WSe_2, ML WS_2, and BL WSe_2/WS_2 prepared on sapphire substrates. (b) Line scanning profile of Raman peak intensity (centered at 309.4 cm^{-1}) acquired from the dashed line labeled in the optical image (inset). (c) Low-frequency Raman spectra taken from WSe_2/WS_2 BL and ML WS_2 on sapphire substrates.

RESULTS AND DISCUSSION

Structure Analysis. High-density MLs of WS_2 and WSe_2 with lateral lengths on the order of tens of micrometers were synthesized directly on SiO_2/Si or *c*-sapphire substrates by reducing WO_3 powder with sulfur (S) or H_2Se, respectively, at elevated temperatures, as described in detail in the Methods section. Their triangular shapes, single-crystalline structure, and layer thicknesses were analyzed with optical microscopy, scanning electron microscopy (SEM), transmission electron microscopy (TEM), and AFM (see Figures S1 and S2 in the Supporting Information). Twisted WSe_2/WS_2 BLs were fabricated by stamping ML WS_2 onto ML WSe_2 with a polymer-assisted approach, followed by a postanneal. Briefly, to prepare WSe_2/WS_2 bilayer samples, triangular WS_2 MLs were first detached from a growth substrate with a poly(methyl methacrylate) (PMMA) film in KOH etchant. Next, the PMMA film containing WS_2 flakes was stamped onto a target substrate (either SiO_2/Si or sapphire) having a high density of WSe_2 MLs. To remove the PPMA and the residue, the as-transferred sample was dipped into acetone and then annealed in an Ar/H_2 ambient at 350 °C (see Methods section). The high yield of CVD-grown triangular flakes enables us to obtain a number of WS_2/WSe_2 BLs with different twist angles (θ) on sapphire or SiO_2/Si substrates (Figure S3). Figure 1a illustrates a WSe_2/WS_2 BL constructed by stacking a ML of WS_2 onto a ML of WSe_2 with a twist angle of 25.3°. As displayed in the optical micrograph (Figure 1b), optical contrast exists between the BL junction areas, each individual ML, and the Si/SiO_2 substrate. The heterojunction region was further examined using AFM, and Figure 1c shows a typical image with a cross-sectional height profile of a postannealed WSe_2/WS_2 BL. A step height of ~0.8 nm corresponds to the thickness of a WS_2 ML stacked on a WSe_2 ML. Prior to annealing, a step height of ~1.2 nm was measured, indicating that the two layers were decoupled (Figure S4). Occasionally, corrugated structures were observed where the flakes overlapped, possibly resulting from evaporation of water trapped at the interfaces during stamping. These corrugated structures also have been observed in artificially stacked WSe_2/MoS_2 BLs where incommensurate stacking during annealing was suggested.[13] Despite these findings, the annealing procedure (see Methods section) was highly effective in removing adsorbates and polymer residues, as well as ensuring the vdW coupling between the MLs. We have also examined the AFM and optical images of WSe_2/WS_2 BLs prepared on a SiO_2/Si substrate before and after annealing and found that the twist angles have an experimental uncertainty of ±0.5° (Figure S5).

One concern during annealing of transferred BLs is the formation of alloyed structures or other structural defects resulting from possible chemical reactions between the two MLs. To rule out this possibility in the present case, we have conducted TEM analysis on our artificially stacked BL, and Figure 1d shows an image of the boundary. In contrast to the simple hexagonal lattice observed in the WS_2 ML (Figure 1e), a fast Fourier transform (FFT) filtered HRTEM image (Figure 1f) yields moiré fringes with a spatial envelope periodicity that was 3 to 4 times the lattice constant of WSe_2 (as observed in WS_2/WSe_2 junction area). Measuring the two hexagonal reciprocal lattices in Figure 1f reveals a twist angle of 20° for this particular BL. Theoretically, this should yield a periodicity of 3.5 in the moiré pattern and agrees well with that observed in the HRTEM images. Lastly, two sets of well-defined spots associated with WS_2 and WSe_2 MLs in the FFT images exclude the possibility of chemical reactions taking place at the interface during annealing.

Raman Scattering. Figure 2a shows typical Raman spectra taken from a WSe_2/WS_2 BL and its constituent MLs (note that sapphire was the substrate in all cases). Although the Raman spectrum of the WS_2/WSe_2 BL is roughly a superposition of the spectra of individual WS_2 and WSe_2 MLs, additional features point to interlayer coupling. The A_{1g} shoulder normally observed at 261 cm^{-1} in WSe_2, for example, was red-shifted

DOI: 10.1021/acsnano.6b01486
ACS Nano 2016, 10, 6612−6622

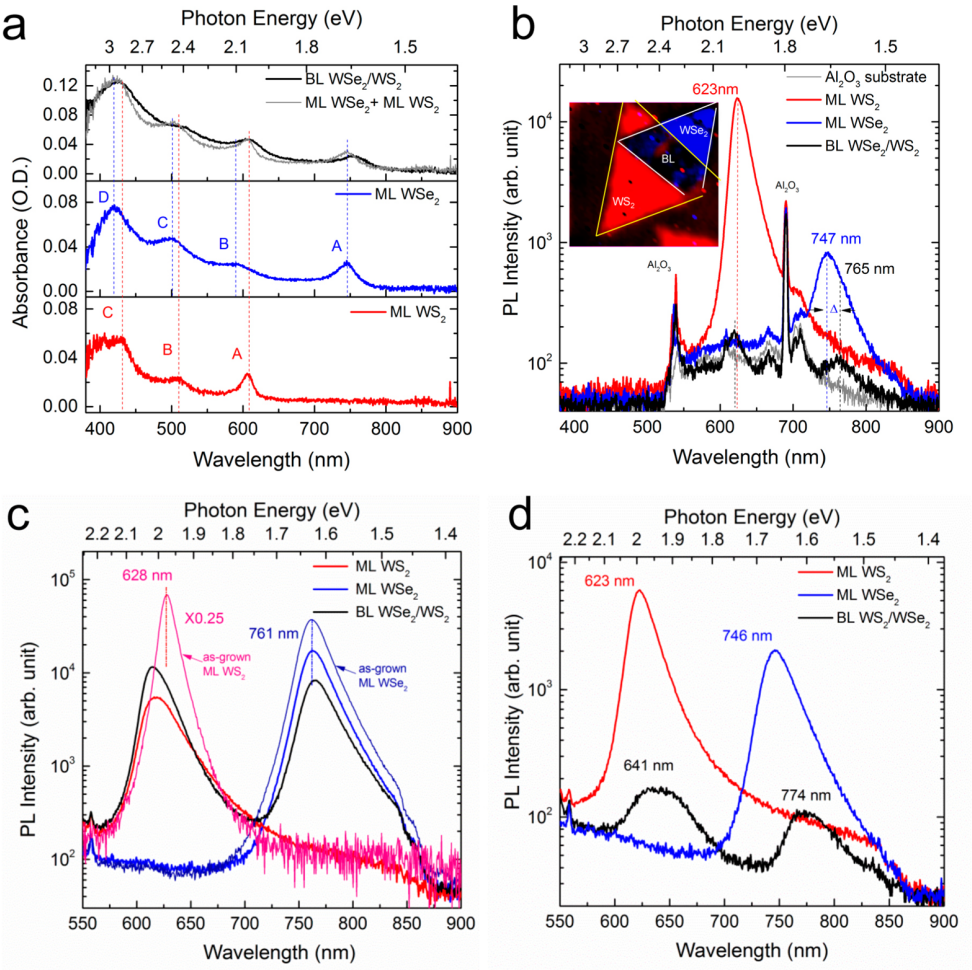

Figure 3. Light absorption and emission characteristics of WSe_2/WS_2 BLs. (a and b) Absorption and PL spectra taken from ML WSe_2, ML WS_2, and WSe_2/WS_2 BLs on a sapphire substrate. Inset in (b) is a PL map of a WSe_2/WS_2 BL. Scale bar is 2 μm. (c and d) PL spectra taken from ML WSe_2, ML WS_2, and WSe_2/WS_2 BLs on a SiO_2/Si substrate before and after annealing.

by ~2 cm^{-1} in the case of the WSe_2/WS_2 BL. This mode in WSe_2 generally red-shifts as the layer number increases,[35,36] indicating interlayer coupling between WS_2 and WSe_2. In contrast, none of the peaks associated with WS_2 were shifted in the BL case; instead, a new peak was noted at 309.4 cm^{-1}. This peak appears only in multilayer WSe_2,[36] indicating that stamping of WS_2 and WSe_2 MLs followed by annealing results in van der Waals coupling analogous to BL WSe_2. Indeed, a line scan across the sample (Figure 2b) measuring the peak intensity at 309.4 cm^{-1} showed the appearance of this additional peak in the WSe_2/WS_2 BL and its absence in the ML WS_2, confirming that it is associated with interlayer coupling. In addition, acquisition of Raman spectra on 10 WSe_2/WS_2 BLs with different twist angles (not shown here) all showed this signature peak. We note that a similar peak was recently observed in the Raman spectra of WSe_2/MoS_2 BLs,[13] suggesting that this may be a general signature for strongly coupled BL systems.

The LF shear and breathing modes (<50 cm^{-1}) reflect in-plane and out-of-plane vibrations of TMD layers. These modes are very sensitive to interlayer coupling and are considered as fingerprints to decode the layer numbers and the atomistic stacking configurations in multilayer TMDs.[37−41] In general, TMD BLs were shown to exhibit one shear and one breathing mode in the LF spectral range.[17,39,42] As shown in the upper panel of Figure 2c, we also observed a Raman feature at ~27 cm^{-1} in WSe_2/WS_2 BL regions in the LF spectral range, which can be further fitted by two peaks, 27.5 ± 1 and 21.5 ± 1 cm^{-1}. The ML region of the stacked WSe_2 crystal shows no Raman modes in the low-frequency range. However, the WS_2 MLs exhibit a Raman feature at 28.7 cm^{-1} showing a band shape similar to that observed for WSe_2/WS_2 bilayers (lower panel in Figure 2c). This LF Raman mode in WS_2 monolayers was noticed before, and its origin still remains unexplained and requires further studies.[41] As shown in Figure S6, this Raman feature appears in CVD-grown and transferred (without and with annealing) WS_2 MLs on SiO_2/Si substrates, which makes definite assignment of the observed LF Raman lines in the case of WSe_2/WS_2 bilayers difficult.

Absorption and Emission Spectroscopy. In order to obtain information on the band structure of the heterobilayers, we further characterized the optical properties of the WSe_2/WS_2 BLs using microabsorption and PL spectroscopies. Microabsorption measurements were performed on MLs of WS_2 and WSe_2 and WSe_2/WS_2 BLs that were synthesized on sapphire substrates. Figure 3a shows the absorption spectra of the MLs as well as the BL, which are similar to those studied previously.[40,43,44] The WS_2 ML exhibited three excitonic

DOI: 10.1021/acsnano.6b01486
ACS Nano 2016, 10, 6612−6622

absorption peaks (labeled A, B, and C), while ML WSe_2 exhibited four (labeled A through D). The excitonic A and B peaks in WS_2 and WSe_2 MLs come from transitions between the spin−orbit split valence band and the lowest conduction band at the K and K′ points of the Brillouin zone.[45] According to the absorption spectra (Figure 3a), the A and B peaks have an energy difference of 392 and 436 meV for WS_2 and WSe_2 MLs, respectively, which are similar to those previously reported for exfoliated and CVD-grown MLs of WS_2 and WSe_2.[46,47] The strong C absorption peaks at higher photon energies are shown to originate from excitonic transitions near the Λ point in K space, where the absorbance is amplified due to the nesting effect.[45,48,49] The same nesting effect is responsible for a partial increase in absorbance in the D band of monolayer WSe_2.

Four absorption peaks were observed in the WSe_2/WS_2 BLs, with their positions very close to the sum of the BL constituent MLs (gray line in the upper panel in Figure 3a). However, two interesting features appear in the absorption spectra of the BL compared to those of the MLs. First, the excitonic peak A in the BL exhibits a red-shift of 40 meV compared to its position in the WSe_2 ML; second, the absorption peaks are broader in the BL compared to those of the MLs. In addition, BLs exhibit ∼10% enhancements in absorbance compared to the sum of the absorbances of the constituent MLs in the spectral range from 400 to 800 nm (see Figure S7a). Note that independent of twist angle, similar changes were observed in all the BLs (Figure S7b and c).

Previous investigations have shown that the positions of the excitonic peaks in TMDs are quite sensitive to charge doping, strain, and crystal quality.[40] Because the WSe_2 flake is grown directly on sapphire (*i.e.*, no mechanical transfer), we can rule out the possibility that the WSe_2 A excitonic red-shift was induced by the substrate. Therefore, the shift is more appropriately interpreted as a consequence of charge doping or strain, if any, induced after pairing with a ML of WS_2. The broadening observed in the BL excitonic bands, on the other hand, may be attributed to a charge transfer effect due to a nonradiative transition of the intralayer excitons into the interlayer excitons, although we cannot totally exclude the possible contribution from the interfacial impurities that were introduced during the transfer process.[21]

Figure 3b shows PL spectra collected from a WSe_2/WS_2 BL on a sapphire substrate, together with the spectra taken from the individual MLs. WS_2 and WSe_2 MLs show strong PL at 623 nm (2.0 eV) and 746 nm (1.7 eV), respectively, which corresponds to recombination of their respective A excitons. In the heterojunction, however, these peaks are largely suppressed. Quantitative analysis showed that the peak intensities decrease by 1 order and 2 orders of magnitude for the WSe_2 and WS_2, respectively. As shown in the PL map (Figure 3b inset), this trend held for the entire structure; that is, strong photoluminescence was observed from ML WS_2 and WSe_2 during PL mapping, while in the stacked area, the PL was strongly quenched. We also found that the BL emission peak corresponding to the WSe_2 ML showed a red-shift of 40 meV, which is the same as the shift measured from the absorption spectra. Analysis of 25 BLs with different twist angles did not reveal any clear trend of this shift with twist angle and showed that all the shifts were scattered around 40 ± 25 meV (Figure S8a). The BL emission peak corresponding to that in the WS_2 ML did not show any shift, at least within an experimental uncertainty of ±10 meV.

The efficient PL quenching of intralayer excitons was previously reported for several families of TMD heterobilayers fabricated either by stacking of CVD-grown/exfoliated MLs or by direct CVD synthesis.[13,15,16,18,19,29] Simultaneous quenching of both intralayer PL emissions in artificially stacked heterobilayers can originate from charge separation between the MLs due to the formation of a type II heterojunction.[9,15] So in our case, for example, this would mean the transfer of an electron to the WS_2 ML with a hole remaining in the WSe_2 ML upon excitation of the A transition in WSe_2 ML or, conversely, transfer of a hole to the WSe_2 ML with an electron remaining in the WS_2 ML under excitation of the A excitonic transition in WS_2. In principle, the simultaneous quenching of both intralayer PL emissions can be used to quantify the interlayer charge transfer rate. Further analysis of the intralayer PL emissions as a function of twist angle revealed that the magnitudes of the intralayer emission quenching for WSe_2 and WS_2 were quite stable, indicating that the charge transfer rate between WSe_2 and WS_2 is relatively insensitive to twist angle (Figure S8b and c).

To understand the effect of annealing on the PL of heterobilayers, we analyzed the spectra for WSe_2/WS_2 BLs fabricated on SiO_2/Si substrates before and after annealing (Figure 3 c and d). Figure 3c shows the PL spectra of the transferred and as-grown WS_2 and WSe_2 MLs and the WSe_2/WS_2 BL before annealing. After being transferred to a SiO_2/Si substrate from the SiO_2/Si growth substrate, the WS_2 ML showed a decrease in the PL intensity and a blue-shift in its peak position compared to those grown directly on SiO_2/Si substrates by CVD. In contrast, the peak position of the WSe_2 ML PL emission remained the same, although a slight decrease in intensity was observed. The blue-shift of the PL emission in the transferred WS_2 ML can be explained by strain relaxation,[16,50] while the decrease in PL intensity might be due to changes in the dielectric environment introduced during processing, *e.g.*, polymer residues or trapped water. After annealing, we found that the intralayer PL intensity for WS_2 and WSe_2 decreased by a factor of 37 and 18 in the heterojunction area (black curve), respectively. This implies that the two layers were actually decoupled before annealing, a conclusion that agrees with our AFM measurements (see Figure S4). Similar to the BLs prepared on sapphire, both intralayer PL emissions were quenched in the annealed heterojunction area, and the intralayer emission corresponding to ML WSe_2 exhibited a noticeable red-shift of 60 ± 2 meV, which further confirmed efficient charge separation in the WSe_2/WS_2 heterojunctions. We also observed that the substrate (sapphire or SiO_2/Si) influenced the degree of intralayer PL intensity suppression in the WSe_2/WS_2 BLs, despite the fact that the BLs on both substrates were fabricated using the same conditions. This effect was more apparent for WSe_2 on sapphire than on SiO_2/Si, where the intralayer PL intensity decreased by a factor of 18 and 8, respectively. This most likely originated from the different doping level and decay rates of the excitonic transitions induced by the two substrates (sapphire and SiO_2).[51,52]

We have also investigated the optical properties of the inverse structure, *i.e.*, WS_2/WSe_2 BL samples that were prepared on sapphire substrates. Similar light absorption and emission characteristics, *i.e.*, enhancement in absorption, quenching of interlayer PL intensity, and red-shift of the WSe_2 A excitonic band in BLs, were observed (Figure S9a and b). Because of the energy difference between the interfaces of

DOI: 10.1021/acsnano.6b01486
ACS Nano 2016, 10, 6612−6622

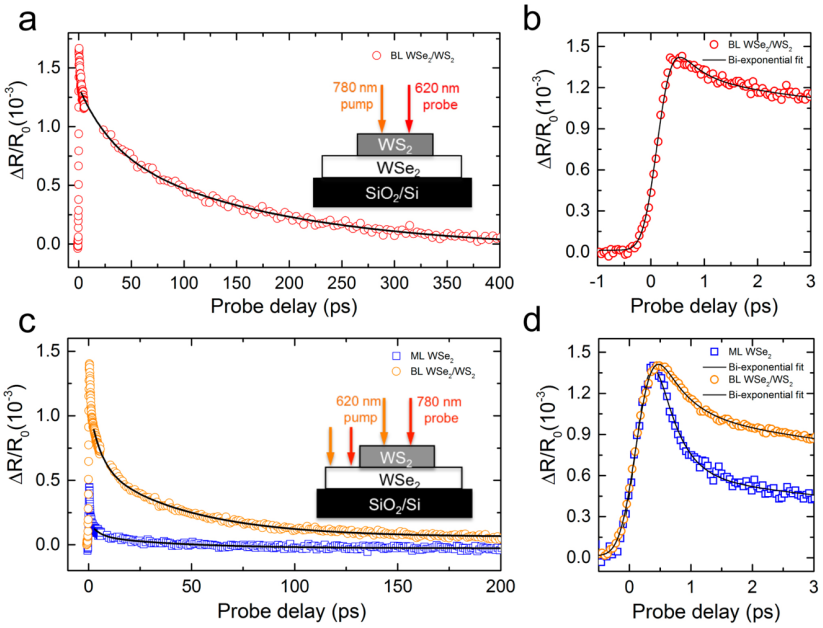

Figure 4. Interlayer transition dynamics in WSe_2/WS_2 BL. (a) Differential reflection *signal* measured from a WSe_2/WS_2 BL with a 780 nm pump and a 620 nm probe pulse. The black line indicates a biexponential *decay* fit with time constants of 21 and 119 ps. (b and d) Differential reflection signal in *the early time delay*. (c) Differential reflection *signal* measured from a WSe_2/WS_2 BL with a 620 nm pump and a 780 nm probe pulse. The black line indicates a biexponential *decay* fit. Insets of (a) and (c) illustrate the corresponding pump−probe configurations.

Al_2O_3/WS_2 and Al_2O_3/WSe_2, Al_2O_3 is assumed to inject different numbers of electrons into WS_2/WSe_2 and WSe_2/WS_2, thus inducing a different magnitude of change in the optical properties between the two structures (Figure S9c). However, compared to the change induced by charge separation (facilitated by the type II heterojunction), the substrate-induced change in optical properties of the heterobilayers is relatively small. Therefore, we observed similar optical characteristics in both structures.

Femtosecond Transient Absorption Spectroscopy. The charge transfer dynamics at the vdW interface were studied using femtosecond transient absorption spectroscopy in reflection geometry. First, the electron transfer from WSe_2 to WS_2 was studied by exciting a BL with a ∼300 fs pump pulse having a central wavelength of 780 nm and an energy fluence of ∼0.9 $\mu J\ cm^{-2}$. Since the photon energy equals the WSe_2 exciton A energy, but is lower than the WS_2 exciton A energy, it can only induce excitons in WSe_2. As discussed above, electrons in WSe_2 are expected to transfer to WS_2, where the low-energy conduction band states reside. The transferred electrons were monitored by measuring the differential reflection of a probe pulse tuned to the A exciton resonance of WS_2 at 620 nm that was delayed with respect to the pump pulse. Differential reflectance ($\Delta R/R_0$) was defined as the normalized change of the probe reflection induced by the pump (Figure 4a). The decay process of the signal was well described by a biexponential function with two time constants (τ_1 = 21 ps and τ_2 = 119 ps). Further measurements with different pump energy fluences showed that the dynamics were independent of fluence in the range of ∼0.2 to ∼5.6 $\mu J\ cm^{-2}$ (Supporting Information Figure S10a and b). These measurements also showed that the amplitude of the differential reflection signal scaled linearly with the pump energy fluence, which confirmed a negligible contribution from nonlinear excitation processes, such as two-photon absorption. From the initial portion of the data shown in Figure 4b, one can see that the differential reflection signal reached its maximum amplitude on a sub-picosecond time scale, revealing the ultrafast electron transfer process. Since the width of the cross correlation of the pump and probe pulses is about 450 fs (see Figure S11), the observed rise time is limited by the instrument response. Hence, the charge transfer time is much shorter than the instrument response time. To rule out the possibility that the detected signal was due to higher energy excitons in WSe_2, we repeated the measurement on a WSe_2 ML triangular flake and observed no signal. This further confirmed that the depletion observed at 620 nm in the case of the WS_2/WSe_2 heterojunction was due to electron transfer from WSe_2 to WS_2.

Lastly, the hole transfer dynamics in the heterobilayers were studied using a 620 nm pump pulse (energy fluence = 2.86 $\mu J\ cm^{-2}$) to generate electron−hole pairs in both layers and a 780 nm probe pulse to monitor the differential reflection around the WSe_2 A exciton resonance. For comparison, the exciton dynamics of ML WSe_2 were also studied under the same conditions. The representative differential reflection signals measured from a WSe_2/WS_2 BL and a WSe_2 ML are shown in Figure 4c. Both signals were fit with a biexponential decay function (black lines in Figure 4c) with a fast decay time constant of 3.0 ps (3.7 ps) and a slow decay time constant of 29.8 ps (31.3 ps) for the BL (ML). Three distinct features were also found by comparing these kinetics. First, the signal amplitude in the BL was 5 times greater than that in ML WSe_2, and this signal was proportional to the pump energy fluence (Figure S10c), which indicates a negligible contribution from nonlinear excitation processes. Second, as shown in Figure 4d, the leading edges of the kinetic traces observed in the WSe_2/WS_2 BL and ML WSe_2 agreed after normalizing their maximum amplitudes (within errors determined by the signal/noise ratio). This shows that the hole transfer process is faster than the time resolution of the measurement. Third, the initial decay

DOI: 10.1021/acsnano.6b01486
ACS Nano 2016, 10, 6612−6622

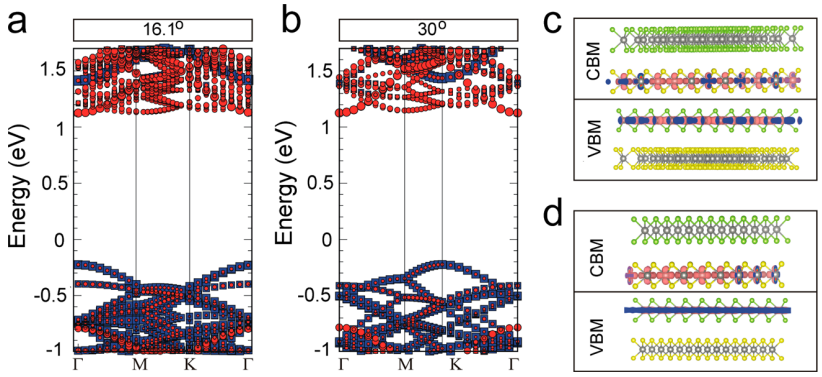

Figure 5. First-principles electronic band structures of WSe_2/WS_2 BLs. The band structures of WSe_2/WS_2 heterojunctions at (a) 16.1° and (b) 30° twist angles, where red and blue colors represent the states from WS_2 and WSe_2, respectively. The charge density distributions of CBM and VBM in (a) and (b) are plotted in (c) and (d), respectively. The green, gray, and yellow atoms represent Se, W, and S atoms, respectively. The red and blue isosurfaces represent positive and negative charge density, for each, with the isosurface density of 0.05 e/A^3.

of the signal from the BL is slower than that of the WSe_2 ML, which may suggest the formation of indirect excitons in the heterobilayers. Since both WSe_2 B and WS_2 A excitons are simultaneously excited with the 620 nm pump pulse, we expect the occurrence of hole transfer from WS_2 to WSe_2 and electron transfer from WSe_2 to WS_2.

First-Principles Electronic Structures Depending on Interlayer Coupling. Although strong quenching of the PL in the heterobilayers indicated efficient charge transfer, we did *not* observe any new absorption or PL peaks, or angular dependence thereof, in the spectral range from 400 to 900 nm. It is interesting to note that the mechanisms and twist angle dependences of the interlayer exciton emission in TMD heterobilayers are still under theoretical debate,[49,53,54] and experimental results tend to be inconsistent.[13,14,16,18,27,29] For example, some calculations have concluded that the interlayer transition in TMD heterojunctions is indirect with negligibly small intensity,[55,56] while in other theoretical predictions TMD heterobilayers have a direct band gap at some specific twist angles or layer combinations.[32,54] Experimentally, on the other hand, several reports involving PL spectroscopy have shown interlayer transitions that are either indirect[13,14,18] or direct,[13,14,23,24] further adding to the confusion. However, some reports have shown that epitaxially grown MoS_2/WS_2 heterostructures (twist angles 0° or 60°) displayed noticeable interlayer exciton peaks at 1.5 and 1.42 eV in the PL spectra,[23,24] while no peaks were found in their CVD-grown artificially stacked counterparts. It was suggested in the latter case that the imperfect interface (due to etchants, *etc.*) between the MLs was responsible for the results.[9,24] For mechanically exfoliated WSe_2/MoS_2 and $WSe_2/MoSe_2$ heterostructures, however, interlayer excitons have been reported, but no dependence of the emission on the relative orientation of the two TMD MLs was found.[14,18]

We are therefore motivated to theoretically explore any potential correlations between electronic properties (band structures) and structure parameters (twist angles and interlayer spacings) by using DFT. Our goal is to understand our experimental data showing no significant role of twist angles on the PL spectrum. We constructed atomic configurations of WSe_2/WS_2 BLs with nine different twist angles ranging from 13.9° to 46.1°. At each angle several different initial stacking configurations were selected to determine the ground-state structure, where the structure was fully optimized by using either local-density approximation (LDA) or Perdew−Burke−Ernzerhof (PBE) + vdW functionals. The optimized interlayer spacing ranges between ∼3.3 and ∼3.5 Å depending on the choice of DFT functionals and rotational angles. The in-plane dimension of the heterojunction supercell was constructed to accommodate WSe_2 and WS_2 of different lattice constants, with computationally tractable system sizes containing no more than 400 atoms at different twist angles and possibly for some small strains (<1.5%) induced by the lattice mismatch between the WSe_2 and WS_2 MLs. This corresponds to the assumption that interlayer vdW interactions are sufficiently strong to enforce registry between the WSe_2 and WS_2 MLs. As both WSe_2 and WS_2 lattices are hexagonal, the WSe_2/WS_2 supercell was also hexagonal with a primitive lattice vector $\vec{C}$ that can be written as $\vec{C} = n_1\vec{a}_1 + n_2\vec{a}_2 = (1 + \varepsilon)\theta(n_1\vec{b}_1 + n_2\vec{b}_2)$. Here, $\vec{a}_1$ and $\vec{a}_2$ are the lattice vectors for WSe_2, $\vec{b}_1$ and $\vec{b}_2$ are the lattice vectors for WS_2, and θ is the twist angle between the WS_2 and WSe_2 MLs (Figure S12).

The WSe_2/WS_2 heterojunction band structures at 16.1° and 30.0°, as examples, are plotted in Figure 5a and b, which represent direct- and indirect-gap cases, respectively. The calculated binding energy between WS_2 and WSe_2 also depends on the twist angles (Figure S13) with a variation of <6 meV/atom. From their band structures as well as charge densities (Figure 5c and d), the valence band maximum (VBM) is mostly due to the in-plane W d_{xy} + $d_{x^2-y^2}$ orbitals in the WSe_2 layer, while the conduction band minimum (CBM) contributions stem primarily from the out-of-plane W d_{z^2} orbitals in the WS_2 layer. These heterojunctions all possess strong type II band alignments that are independent of the twist angle and nature of the band gap, *i.e.*, direct or indirect.

The electronic band gaps of the vertically stacked WSe_2/WS_2 junctions with various twist angles range from ∼1.2 to ∼1.45 eV for both PBE + vdW and LDA. However, the band gap nature of WSe_2/WS_2 can be either direct or indirect, depending on the local atomic configurations determined by either twist angles or interlayer spacing. A slight difference in optimized structures from different DFT functionals, such as LDA and PBE + vdW, will change the local symmetry and interlayer spacing and consequently result in differences in the band gap as well as its nature (direct *vs* indirect). For example, PBE + vdW predicts direct band gaps for a few twist angle configurations, while LDA identifies no direct band gap

DOI: 10.1021/acsnano.6b01486
ACS Nano 2016, 10, 6612−6622

configurations among the considered ones (see Supporting Information Figure S14 for details). Note that the functional dependence of the interlayer spacing has been also reported in the BL MoS_2 structure.[57]

Interlayer spacing is found to be the most prominent factor in determining energy gaps as well as their nature (see Supporting Information). In general, we found indirect to direct band gap transitions as interlayer distance increases, which is valid for both functionals. However, the exact transition point is not absolute, and the region encompassed by the red box in Figure S14b indicates the range of energy gaps arising from optimized configurations at different twist angles, revealing that the strength of the interlayer interaction lies between noninteracting and strongly interacting and depends sensitively on the exact atomistic configuration. Within this region, the characteristics of the bands are easily changed depending on local orbital interactions, producing very subtle changes in the local orbital interaction that precludes clear trends for indirect *vs* direct band gap predictions. Therefore, we find no clear twist angle dependence on direct *vs* indirect band gap is predictable from first-principles calculations, however confirm that robust type II heterojunctions are formed for all optimized configurations, in agreement with experimental results.

CONCLUSION

In conclusion, optical spectroscopy measurements were used to characterize interlayer coupling in bilayers of WSe_2/WS_2 that were synthesized by artificially stacking monolayers of CVD-grown WS_2 onto WSe_2. Raman spectroscopy confirmed interlayer coupling in WSe_2/WS_2 BLs that was manifested by the emergence of a layer-number-sensitive mode at 309.4 cm^{-1} analogous to that observed for few-layer WSe_2. The interlayer interaction was found to induce efficient spatial charge separation and enhanced light absorption at the WSe_2/WS_2 vdW interface, resulting in a shift and broadening of the characteristic monolayer excitonic absorption bands and a ~10% increase in integrated absorbance across the visible spectrum for the bilayer compared to the sum of the individual monolayer spectra. Rapid interlayer charge transfer indicated by the spectral broadening near the A exciton band-edge of WSe_2 was further supported by the induced absorption dynamics measured by ultrafast pump−probe spectroscopy. The long recombination time observed in the hole transfer dynamic study suggests the formation of an interlayer exciton, and strong quenching of the PL intensity of the bilayers compared to the individual layers indicated that nonradiative channels dominate de-excitation pathways. Although our density functional calculations identified particular atomistic arrangements that should result in noticeable variations in direct and indirect band gaps for different interlayer twist angles, importantly, optical spectroscopy revealed that the interlayer coupling in the stamped heterostructures is relatively insensitive to twist angle, indicating that such arrangements are experimentally highly unlikely. Significantly, the experimental confirmation of robust type II heterojunctions for all twist-angle configurations of the WSe_2/WS_2 BLs is highly encouraging for the potential realization of reliable optoelectronic devices such as solar cells and photodetectors by the stamping approach.

METHODS

WS_2 and WSe_2 ML Synthesis. MLs of WS_2 and WSe_2 were grown separately on *c*-plane sapphire or silicon substrates with a 300 nm dielectric layer of thermal oxide (SiO_2/Si) by chemical vapor deposition in a horizontal tube furnace. For samples grown on sapphire, an alumina crucible with WO_3 powders was positioned at the center of the tube furnace, while the sapphire substrate was located downstream next to the crucible. Sulfur or selenium pellets were placed in a separate crucible upstream in a zone of the tube furnace warmed by heating tape. When the temperature at the center of the furnace reached 920 °C, a mixed gas flow of argon and hydrogen was used to transfer sulfur or selenium vapor to the center of the tube furnace to reduce the WO_3 powder. During growth, the pressure was maintained at 0.5 and 5.0 Torr for WS_2 and WSe_2, respectively. Prior to growth, the sapphire substrate was annealed at 1100 °C for 10 h in order to produce a flat surface. For samples grown on SiO_2/Si substrates, the pressure was maintained at ambient pressure, and the temperature for growth of WS_2 and WSe_2 was set to 800 °C. After the tube furnace was naturally cooled to room temperature, ML WS_2 or WSe_2 flakes were characterized by structural analysis and optical measurements.

Fabrication of WSe_2/WS_2 BLs. BLs were prepared using a PMMA stamping method as follows: To prepare WSe_2/WS_2 hybrid structures, WS_2 flakes grown on sapphire were first spin-coated with PMMA (A4), leaving a ~100 nm thick polymer film. After being cured at 100 °C for 15 min, the PMMA/WS_2 sample was detached from the sapphire substrate with a 30% KOH solution (100 °C and 0.5−1.0 h). The sample was then transferred to DI water to reduce the KOH residue. Afterward, the PMMA/WS_2 was transferred onto ML WSe_2 grown on a sapphire substrate, followed by preheating with a hot plate at 100 °C for 5 min. Finally, the as-prepared WSe_2/WS_2 samples were annealed at 350 °C in a Ar flow (90 sccm, 10 Torr) for 3 h in order to remove the polymer residue.

Structure Characterization (SEM, TEM, and AFM). To prepare the WSe_2/WS_2 sample for TEM analysis, the same procedure described previously was used to detach the hybrid layers from the sapphire. After washing in DI water for 10 min, the PMMA film with flakes was transferred to a QUANTIFOIL TEM grid. To remove the polymer, the TEM grids were then annealed in an Ar environment as described above. HRTEM and EELS studies were carried out on a Zeiss Libra 200 MC transmission electron microscope, operated at an accelerating voltage of 200 kV. (Information limit in Libra HRTEM mode is 1 Å.) The height profiles of the MLs and hybrid layer were measured by AFM (Bruker Dimension Icon).

Optical Characterizations (Raman, PL, PL Mapping, and Absorption Measurements). Photoluminescence spectra were measured with a 532 nm solid-state laser excitation source. The laser beam was focused to a spot size of ~1 μm to excite the ML WSe_2, ML WS_2, and the WSe_2/WS_2 hybrid layers. The PL signals were recorded with a monochromator and a liquid-nitrogen-cooled charge-coupled device (CCD). Two-dimensional PL mapping was carried out by scanning a computer-controlled stage. The Raman spectra were acquired using a micro-Raman system based on a Jobin-Yvon T64000 triple spectrometer equipped with 1800 grooves per millimeter gratings and a liquid-nitrogen-cooled CCD detector (Symphony Horiba JY). To measure the absorption spectra of the MLs and BLs, a laser-driven light source (EQ-99-fc, Energetiq) was used (focused spot size at the sample was ~2 μm). The transmitted light was captured with a microscope objective (50×, NA = 0.5) and directed to a spectrometer (Spectra Pro 2300i, Acton) equipped with a CCD camera (Pixis 256BR, Princeton Instruments). The absorbance (A) was calculated as $A = \log_{10}(I_0/I)$, where I and I_0 are the light intensities transmitted through the sapphire substrate on and off a TMD crystal, respectively. All the spectra and maps were collected at room temperature.

Femtosecond Transient Absorption Spectroscopy. In the differential reflection setup, a diode laser with a wavelength of 532 nm and a power of 8.5 W was used to pump a Ti:sapphire laser, which generates ultrashort pulses with a central wavelength of 780 nm, a repetition rate of about 80 MHz, and an average power of 2.0 W. To obtain the 620 nm pulses, supercontinnum generation from a photonic crystal fiber, pumped with part of the Ti:sapphire output, was utilized. A bandpass filter was used to select the desired spectral component. In

DOI: 10.1021/acsnano.6b01486
ACS Nano 2016, 10, 6612−6622

each of the measurements, the pump and probe beams were linearly polarized along perpendicular directions and then combined by a beamsplitter and focused onto the sample by a microscope objective lens with a numerical aperture of 0.4. The focused spot sizes of the pump and probe were 1−2 μm fwhm, determined by an imaging system. The reflection of the probe from the sample was collimated by the objective lens and sent to a biased silicon photodiode. The pump, however, was prevented from reaching the detector by a set of filters. A lock-in amplifier measured the output of the photodiode, with the intensity of the pump beam modulated at ∼2 kHz by a mechanical chopper. The differential reflection was measured as a function of the probe delay, which was controlled by varying the length of the pump path with a linear stage.

Density Functional Calculations. All the DFT calculations were performed using the VASP code.[58] Projector augmented wave potentials were used to describe the core electrons, and the generalized gradient approximation with the PBE-type functional was selected in our calculations. The effect of vdW interactions was taken into account by using the PBE + vdW scheme, where C6 coefficients are obtained based on self-consistent electron density.[59] In order to the test the functional dependence on the electronic and structural properties, we also performed calculations employing the LDA for the exchange−correlation functional as parametrized by Perdew and Zunger.[60] The kinetic energy cutoff for the plane-wave basis was set to 400 eV. The structure was fully relaxed until the force on each atom was less than 0.01 eV/A.

ASSOCIATED CONTENT

Supporting Information

The Supporting Information is available free of charge on the ACS Publications website at DOI: 10.1021/acsnano.6b01486.

Structural analyses of the MLs of WS_2 and WSe_2, annealing effect on the BL morphologies, more optical data analysis, detailed analysis about the charge transfer dynamics, and the comparison between LDA and PBE + vdW for interlayer exciton band structure calculations (PDF)

AUTHOR INFORMATION

Corresponding Authors

*E-mail: wangk@ornl.gov.
*E-mail: geohegandb@ornl.gov.

Notes

The authors declare no competing financial interest.

ACKNOWLEDGMENTS

Research was supported by the U.S. Department of Energy, Office of Science, Basic Energy Sciences (BES), Materials Sciences and Engineering Division, and performed in part as a user project at the Center for Nanophase Materials Sciences (CNMS), which is a DOE Office of Science User Facility. Characterization techniques and spectroscopic facilities at CNMS developed through the CNMS theme science program. K.W. thanks Dr. Ying-Zhong Ma for his suggestion on exciton dynamics studies. This article has been authored by UT-Battelle, LLC, under Contract No. DE-AC05-00OR22725 with the U.S. Department of Energy. The United States Government retains and the publisher, by accepting the article for publication, acknowledges that the United States Government retains a nonexclusive, paid-up, irrevocable, worldwide license to publish or reproduce the published form of this article, or allow others to do so, for United States Government purposes. The Department of Energy will provide public access to these results of federally sponsored research in accordance with the DOE Public Access Plan (http://energy.gov/downloads/doe-public-access-plan).

REFERENCES

(1) Mak, K. F.; Lee, C.; Hone, J.; Shan, J.; Heinz, T. F. Atomically Thin MoS_2: A New Direct-Gap Semiconductor. *Phys. Rev. Lett.* **2010**, *105*, 136805.

(2) Zhang, Y.; Chang, T.-R.; Zhou, B.; Cui, Y.-T.; Yan, H.; Liu, Z.; Schmitt, F.; Lee, J.; Moore, R.; Chen, Y.; Lin, H.; Jeng, H.-T.; Mo, S.-K.; Hussain, Z.; Bansil, A.; Shen, Z.-X. Direct Observation of the Transition from Indirect to Direct Bandgap in Atomically Thin Epitaxial $MoSe_2$. *Nat. Nanotechnol.* **2014**, *9*, 111−115.

(3) Radisavljevic, B.; Radenovic, A.; Brivio, J.; Giacometti, V.; Kis, A. Single-Layer MoS_2 Transistors. *Nat. Nanotechnol.* **2011**, *6*, 147−150.

(4) Perkins, F. K.; Friedman, A. L.; Cobas, E.; Campbell, P. M.; Jernigan, G. G.; Jonker, B. T. Chemical Vapor Sensing with Mono Layer MoS_2. *Nano Lett.* **2013**, *13*, 668−673.

(5) Wu, S.; Buckley, S.; Schaibley, J. R.; Feng, L.; Yan, J.; Mandrus, D. G.; Hatami, F.; Yao, W.; Vuckovic, J.; Majumdar, A.; Xu, X. Monolayer Semiconductor Nanocavity Lasers with Ultralow Thresholds. *Nature* **2015**, *520*, 69−72.

(6) Wu, W.; Wang, L.; Li, Y.; Zhang, F.; Lin, L.; Niu, S.; Chenet, D.; Zhang, X.; Hao, Y.; Heinz, T. F.; Hone, J.; Wang, Z. L. Piezoelectricity of Single-Atomic-Layer MoS_2 for Energy Conversion and Piezotronics. *Nature* **2014**, *514*, 470−474.

(7) Zhu, H.; Wang, Y.; Xiao, J.; Liu, M.; Xiong, S.; Wong, Z. J.; Ye, Z.; Ye, Y.; Yin, X.; Zhang, X. Observation of Piezoelectricity in Free-Standing Monolayer MoS_2. *Nat. Nanotechnol.* **2015**, *10*, 151−155.

(8) Kang, J.; Tongay, S.; Zhou, J.; Li, J.; Wu, J. Band Offsets and Heterostructures of Two-Dimensional Semiconductors. *Appl. Phys. Lett.* **2013**, *102*, 012111.

(9) Zhu, X.; Monahan, N. R.; Gong, Z.; Zhu, H.; Williams, K. W.; Nelson, C. A. Charge Transfer Excitons at Van Der Waals Interfaces. *J. Am. Chem. Soc.* **2015**, *137*, 8313−8320.

(10) Huang, S.; Ling, X.; Liang, L.; Kong, J.; Terrones, H.; Meunier, V.; Dresselhaus, M. S. Probing the Interlayer Coupling of Twisted Bilayer MoS_2 Using Photoluminescence Spectroscopy. *Nano Lett.* **2014**, *14*, 5500−5508.

(11) Liu, K.; Zhang, L.; Cao, T.; Jin, C.; Qiu, D.; Zhou, Q.; Zettl, A.; Yang, P.; Louie, S. G.; Wang, F. Evolution of Interlayer Coupling in Twisted Molybdenum Disulfide Bilayers. *Nat. Commun.* **2014**, *5*, 4966.

(12) Yan, W.; Meng, L.; Liu, M.; Qiao, J.-B.; Chu, Z.-D.; Dou, R.-F.; Liu, Z.; Nie, J.-C.; Naugle, D. G.; He, L. Angle-Dependent Van Hove Singularities and Their Breakdown in Twisted Graphene Bilayers. *Phys. Rev. B: Condens. Matter Mater. Phys.* **2014**, *90*, 115402.

(13) Chiu, M.-H.; Li, M.-Y.; Zhang, W.; Hsu, W.-T.; Chang, W.-H.; Terrones, M.; Terrones, H.; Li, L.-J. Spectroscopic Signatures for Interlayer Coupling in MoS_2-WSe_2 Van Der Waals Stacking. *ACS Nano* **2014**, *8*, 9649−9656.

(14) Fang, H.; Battaglia, C.; Carraro, C.; Nemsak, S.; Ozdol, B.; Kang, J. S.; Bechtel, H. A.; Desai, S. B.; Kronast, F.; Unal, A. A.; Conti, G.; Conlon, C.; Palsson, G. K.; Martin, M. C.; Minor, A. M.; Fadley, C. S.; Yablonovitch, E.; Maboudian, R.; Javey, A. Strong Interlayer Coupling in Van Der Waals Heterostructures Built from Single-Layer Chalcogenides. *Proc. Natl. Acad. Sci. U. S. A.* **2014**, *111*, 6198−6202.

(15) Hong, X.; Kim, J.; Shi, S.-F.; Zhang, Y.; Jin, C.; Sun, Y.; Tongay, S.; Wu, J.; Zhang, Y.; Wang, F. Ultrafast Charge Transfer in Atomically Thin MoS_2/WS_2 Heterostructures. *Nat. Nanotechnol.* **2014**, *9*, 682−686.

(16) Tongay, S.; Fan, W.; Kang, J.; Park, J.; Koldemir, U.; Suh, J.; Narang, D. S.; Liu, K.; Ji, J.; Li, J. B.; Sinclair, R.; Wu, J. Q. Tuning Interlayer Coupling in Large-Area Heterostructures with CVD-Grown MoS_2 and WS_2 Monolayers. *Nano Lett.* **2014**, *14*, 3185−3190.

(17) Lui, C. H.; Ye, Z. P.; Ji, C.; Chiu, K. C.; Chou, C. T.; Andersen, T. I.; Means-Shively, C.; Anderson, H.; Wu, J. M.; Kidd, T.; Lee, Y. H.; He, R. Observation of Interlayer Phonon Modes in Van Der Waals Heterostructures. *Phys. Rev. B: Condens. Matter Mater. Phys.* **2015**, *91*, 165403.

DOI: 10.1021/acsnano.6b01486
ACS Nano 2016, 10, 6612−6622

(18) Rivera, P.; Schaibley, J. R.; Jones, A. M.; Ross, J. S.; Wu, S.; Aivazian, G.; Klement, P.; Seyler, K.; Clark, G.; Ghimire, N. J.; Yan, J.; Mandrus, D. G.; Yao, W.; Xu, X. Observation of Long-Lived Interlayer Excitons in Monolayer $MoSe_2$-WSe_2 Heterostructures. *Nat. Commun.* **2015**, *6*, 6242.
(19) Ceballos, F.; Bellus, M. Z.; Chiu, H.-Y.; Zhao, H. Ultrafast Charge Separation and Indirect Exciton Formation in a MoS_2-$MoSe_2$ Van Der Waals Heterostructure. *ACS Nano* **2014**, *8*, 12717−12724.
(20) Lee, C.-H.; Lee, G.-H.; van der Zande, A. M.; Chen, W.; Li, Y.; Han, M.; Cui, X.; Arefe, G.; Nuckolls, C.; Heinz, T. F.; Guo, J.; Hone, J.; Kim, P. Atomically Thin P-N Junctions with Van Der Waals Heterointerfaces. *Nat. Nanotechnol.* **2014**, *9*, 676−681.
(21) Rigosi, A. F.; Hill, H. M.; Li, Y.; Chernikov, A.; Heinz, T. F. Probing Interlayer Interactions in Transition Metal Dichalcogenide Heterostructures by Optical Spectroscopy: MoS_2/WS_2 and $MoSe_2$/WSe_2. *Nano Lett.* **2015**, *15*, 5033−5038.
(22) Hsu, W.-T.; Zhao, Z.-A.; Li, L.-J.; Chen, C.-H.; Chiu, M.-H.; Chang, P.-S.; Chou, Y.-C.; Chang, W.-H. Second Harmonic Generation from Artificially Stacked Transition Metal Dichalcogenide Twisted Bilayers. *ACS Nano* **2014**, *8*, 2951−2958.
(23) Gong, Y.; Lin, J.; Wang, X.; Shi, G.; Lei, S.; Lin, Z.; Zou, X.; Ye, G.; Vajtai, R.; Yakobson, B. I.; Terrones, H.; Terrones, M.; Tay, B. K.; Lou, J.; Pantelides, S. T.; Liu, Z.; Zhou, W.; Ajayan, P. M. Vertical and in-Plane Heterostructures from WS_2/MoS_2 Monolayers. *Nat. Mater.* **2014**, *13*, 1135−1142.
(24) Heo, H.; Sung, J. H.; Cha, S.; Jang, B.-G.; Kim, J.-Y.; Jin, G.; Lee, D.; Ahn, J.-H.; Lee, M.-J.; Shim, J. H.; Choi, H.; Jo, M.-H. Interlayer Orientation-Dependent Light Absorption and Emission in Monolayer Semiconductor Stacks. *Nat. Commun.* **2015**, *6*, 7372.
(25) van der Zande, A. M.; Huang, P. Y.; Chenet, D. A.; Berkelbach, T. C.; You, Y.; Lee, G.-H.; Heinz, T. F.; Reichman, D. R.; Muller, D. A.; Hone, J. C. Grains and Grain Boundaries in Highly Crystalline Monolayer Molybdenum Disulphide. *Nat. Mater.* **2013**, *12*, 554−561.
(26) Wang, S.; Rong, Y.; Fan, Y.; Pacios, M.; Bhaskaran, H.; He, K.; Warner, J. H. Shape Evolution of Monolayer MoS_2 Crystals Grown by Chemical Vapor Deposition. *Chem. Mater.* **2014**, *26*, 6371−6379.
(27) Gong, Y.; Liu, Z.; Lupini, A. R.; Shi, G.; Lin, J.; Najmaei, S.; Lin, Z.; Elias, A. L.; Berkdemir, A.; You, G.; Terrones, H.; Terrones, M.; Vajtai, R.; Pantelides, S. T.; Pennycook, S. J.; Lou, J.; Zhou, W.; Ajayan, P. M. Band Gap Engineering and Layer-by-Layer Mapping of Selenium-Doped Molybdenum Disulfide. *Nano Lett.* **2014**, *14*, 442−449.
(28) Huang, C.; Wu, S.; Sanchez, A. M.; Peters, J. J. P.; Beanland, R.; Ross, J. S.; Rivera, P.; Yao, W.; Cobden, D. H.; Xu, X. Lateral Heterojunctions within Monolayer $MoSe_2$-WSe_2 Semiconductors. *Nat. Mater.* **2014**, *13*, 1096−1101.
(29) Yu, Y.; Hu, S.; Su, L.; Huang, L.; Liu, Y.; Jin, Z.; Purezky, A. A.; Geohegan, D. B.; Kim, K. W.; Zhang, Y.; Cao, L. Equally Efficient Interlayer Exciton Relaxation and Improved Absorption in Epitaxial and Nonepitaxial MoS_2/WS_2 Heterostructures. *Nano Lett.* **2015**, *15*, 486−491.
(30) Li, X.; Lin, M.-W.; Lin, J.; Huang, B.; Puretzky, A. A.; Ma, C.; Wang, K.; Zhou, W.; Pantelides, S. T.; Chi, M.; Kravchenko, I.; Fowlkes, J.; Rouleau, C. M.; Geohegan, D. B.; Xiao, K. Two-Dimensional GaSe/$MoSe_2$ Misfit Bilayer Heterojunctions by Van Der Waals Epitaxy. *Sci. Adv.* **2016**, *2*, e1501882.
(31) Li, X.; Basile, L.; Huang, B.; Ma, C.; Lee, J.; Vlassiouk, I. V.; Puretzky, A. A.; Lin, M.-W.; Yoon, M.; Chi, M.; Idrobo, J. C.; Rouleau, C. M.; Sumpter, B. G.; Geohegan, D. B.; Xiao, K. Van Der Waals Epitaxial Growth of Two-Dimensional Single-Crystalline Gase Domains on Graphene. *ACS Nano* **2015**, *9*, 8078−8088.
(32) Terrones, H.; Lopez-Urias, F.; Terrones, M. Novel Hetero-Layered Materials with Tunable Direct Band Gaps by Sandwiching Different Metal Disulfides and Diselenides. *Sci. Rep.* **2013**, *3*, 1549.
(33) Ye, Y.; Wong, Z. J.; Lu, X.; Ni, X.; Zhu, H.; Chen, X.; Wang, Y.; Zhang, X. Monolayer Excitonic Laser. *Nat. Photonics* **2015**, *9*, 733−737.
(34) Zhou, H.; Wang, C.; Shaw, J. C.; Cheng, R.; Chen, Y.; Huang, X.; Liu, Y.; Weiss, N. O.; Lin, Z.; Huang, Y.; Duan, X. Large Area Growth and Electrical Properties of p-Type WSe_2 Atomic Layers. *Nano Lett.* **2015**, *15*, 709−713.
(35) Li, H.; Lu, G.; Wang, Y.; Yin, Z.; Cong, C.; He, Q.; Wang, L.; Ding, F.; Yu, T.; Zhang, H. Mechanical Exfoliation and Characterization of Single- and Few-Layer Nanosheets of WSe_2, TaS_2, and $TaSe_2$. *Small* **2013**, *9*, 1974−1981.
(36) Zhao, W.; Ghorannevis, Z.; Amara, K. K.; Pang, J. R.; Toh, M.; Zhang, X.; Kloc, C.; Tan, P. H.; Eda, G. Lattice Dynamics in Mono- and Few-Layer Sheets of WS_2 and WSe_2. *Nanoscale* **2013**, *5*, 9677−9683.
(37) Ling, X.; Liang, L.; Huang, S.; Puretzky, A. A.; Geohegan, D. B.; Sumpter, B. G.; Kong, J.; Meunier, V.; Dresselhaus, M. S. Low-Frequency Interlayer Breathing Modes in Few-Layer Black Phosphorus. *Nano Lett.* **2015**, *15*, 4080−4088.
(38) Lui, C. H.; Heinz, T. F. Measurement of Layer Breathing Mode Vibrations in Few-Layer Graphene. *Phys. Rev. B: Condens. Matter Mater. Phys.* **2013**, *87*, 121404.
(39) Zhao, Y.; Luo, X.; Li, H.; Zhang, J.; Araujo, P. T.; Gan, C. K.; Wu, J.; Zhang, H.; Quek, S. Y.; Dresselhaus, M. S.; Xiong, Q. Interlayer Breathing and Shear Modes in Few-Trilayer MoS_2 and WSe_2. *Nano Lett.* **2013**, *13*, 1007−1015.
(40) Li, Y.; Chernikov, A.; Zhang, X.; Rigosi, A.; Hill, H. M.; van der Zande, A. M.; Chenet, D. A.; Shih, E.-M.; Hone, J.; Heinz, T. F. Measurement of the Optical Dielectric Function of Monolayer Transition-Metal Dichalcogenides: MoS_2, $MoSe_2$, WS_2 and WSe_2. *Phys. Rev. B: Condens. Matter Mater. Phys.* **2014**, *90*, 205422.
(41) O'Brien, M.; McEvoy, N.; Hanlon, D.; Hallam, T.; Coleman, J. N.; Duesberg, G. S. Mapping of Low-Frequency Raman Modes in CVD-Grown Transition Metal Dichalcogenides: Layer Number, Stacking Orientation and Resonant Effects. *Sci. Rep.* **2016**, *6*, 19476.
(42) Puretzky, A. A.; Liang, L.; Li, X.; Xiao, K.; Wang, K.; Mahjouri-Samani, M.; Basile, L.; Idrobo, J. C.; Sumpter, B. G.; Meunier, V.; Geohegan, D. B. Low-Frequency Raman Fingerprints of Two-Dimensional Metal Dichalcogenide Layer Stacking Configurations. *ACS Nano* **2015**, *9*, 6333−6342.
(43) Huang, J.-K.; Pu, J.; Hsu, C.-L.; Chiu, M.-H.; Juang, Z.-Y.; Chang, Y.-H.; Chang, W.-H.; Iwasa, Y.; Takenobu, T.; Li, L.-J. Large-Area Synthesis of Highly Crystalline WSe_2 Monolayers and Device Applications. *ACS Nano* **2014**, *8*, 923−930.
(44) Peimyoo, N.; Shang, J.; Cong, C.; Shen, X.; Wu, X.; Yeow, E. K. L.; Yu, T. Nonblinking, Intense Two-Dimensional Light Emitter: Monolayer WS_2 Triangles. *ACS Nano* **2013**, *7*, 10985−10994.
(45) Qiu, D. Y.; da Jornada, F. H.; Louie, S. G. Optical Spectrum of MoS_2: Many-Body Effects and Diversity of Exciton States. *Phys. Rev. Lett.* **2013**, *111*, 216805.
(46) Liu, H.-L.; Shen, C.-C.; Su, S.-H.; Hsu, C.-L.; Li, M.-Y.; Li, L.-J. Optical Properties of Monolayer Transition Metal Dichalcogenides Probed by Spectroscopic Ellipsometry. *Appl. Phys. Lett.* **2014**, *105*, 201905.
(47) Zhao, W.; Ghorannevis, Z.; Chu, L.; Toh, M.; Kloc, C.; Tan, P.-H.; Eda, G. Evolution of Electronic Structure in Atomically Thin Sheets of WS_2 and WSe_2. *ACS Nano* **2013**, *7*, 791−797.
(48) Carvalho, A.; Ribeiro, R. M.; Castro Neto, A. H. Band Nesting and the Optical Response of Two-Dimensional Semiconducting Transition Metal Dichalcogenides. *Phys. Rev. B: Condens. Matter Mater. Phys.* **2013**, *88*, 115205.
(49) Debbichi, L.; Eriksson, O.; Lebègue, S. Electronic Structure of Two-Dimensional Transition Metal Dichalcogenide Bilayers from *Ab Initio* Theory. *Phys. Rev. B: Condens. Matter Mater. Phys.* **2014**, *89*, 205311.
(50) Conley, H. J.; Wang, B.; Ziegler, J. I.; Haglund, R. F.; Pantelides, S. T.; Bolotin, K. I. Bandgap Engineering of Strained Monolayer and Bilayer MoS_2. *Nano Lett.* **2013**, *13*, 3626−3630.
(51) Buscema, M.; Steele, G.; van der Zant, H. J.; Castellanos-Gomez, A. The Effect of the Substrate on the Raman and Photoluminescence Emission of Single-Layer MoS_2. *Nano Res.* **2014**, *7*, 561−571.

DOI: 10.1021/acsnano.6b01486
ACS Nano 2016, 10, 6612−6622

(52) Li, Y.; Qi, Z.; Liu, M.; Wang, Y.; Cheng, X.; Zhang, G.; Sheng, L. Photoluminescence of Monolayer MoS_2 on $LaAlO_3$ and $SrTiO_3$ Substrates. *Nanoscale* **2014**, *6*, 15248−15254.
(53) Amin, B.; Singh, N.; Schwingenschlögl, U. Heterostructures of Transition Metal Dichalcogenides. *Phys. Rev. B: Condens. Matter Mater. Phys.* **2015**, *92*, 075439.
(54) Kośmider, K.; Fernández-Rossier, J. Electronic Properties of the MoS_2-WS_2 Heterojunction. *Phys. Rev. B: Condens. Matter Mater. Phys.* **2013**, *87*, 075451.
(55) Kang, J.; Li, J.; Li, S.-S.; Xia, J.-B.; Wang, L.-W. Electronic Structural Moiré Pattern Effects on MoS_2/$MoSe_2$ 2D Heterostructures. *Nano Lett.* **2013**, *13*, 5485−5490.
(56) Komsa, H.-P.; Krasheninnikov, A. V. Electronic Structures and Optical Properties of Realistic Transition Metal Dichalcogenide Heterostructures from First Principles. *Phys. Rev. B: Condens. Matter Mater. Phys.* **2013**, *88*, 085318.
(57) van der Zande, A. M.; Kunstmann, J.; Chernikov, A.; Chenet, D. A.; You, Y.; Zhang, X.; Huang, P. Y.; Berkelbach, T. C.; Wang, L.; Zhang, F.; Hybertsen, M. S.; Muller, D. A.; Reichman, D. R.; Heinz, T. F.; Hone, J. C. Tailoring the Electronic Structure in Bilayer Molybdenum Disulfide *via* Interlayer Twist. *Nano Lett.* **2014**, *14*, 3869−3875.
(58) Kresse, G.; Furthmüller, J. Efficiency of Ab-Initio Total Energy Calculations for Metals and Semiconductors Using a Plane-Wave Basis Set. *Comput. Mater. Sci.* **1996**, *6*, 15−50.
(59) Tkatchenko, A.; Scheffler, M. Accurate Molecular Van Der Waals Interactions from Ground-State Electron Density and Free-Atom Reference Data. *Phys. Rev. Lett.* **2009**, *102*, 073005.
(60) Perdew, J. P.; Zunger, A. Self-Interaction Correction to Density-Functional Approximations for Many-Electron Systems. *Phys. Rev. B: Condens. Matter Mater. Phys.* **1981**, *23*, 5048−5079.

DOI: 10.1021/acsnano.6b01486
ACS Nano 2016, 10, 6612−6622